

Making Use of Labyrinth Interaction Flow

A. Pfau
A. I. Kalfas
R. S. Abhari

Turbomachinery Laboratory,
Swiss Federal Institute of Technology,
8092 Zurich, Switzerland

It is the aim of this publication to attract the designers attention to the end wall flow interactions of shrouded high pressure turbines. One of the key issues for designing better turbines is the understanding of the flow interactions set up by the presence of labyrinth seals. Those interaction flows are carefully examined in this publication using the control volume analysis and the radial equilibrium of forces acting on streamlines. The consequences on secondary flow development and mixing losses are discussed and quantified. Out of this insight, design recommendations are derived, which attempt to make use of the nature of the labyrinth interaction flow. The open labyrinth cavities are classified in a systematic way. The aim of this approach is to work out the characteristic differences between hub and tip cavities and those having a leakage jet or sucking main flow fluid into the labyrinth. The influence on the main flow is discussed in terms of the incidence flow angle of downstream blade rows and the associated loss production mechanisms. The design strategies presented in this paper follow two paths: (a) Optimization of the mixing losses of the leakage jets at hub and tip is estimated to result in an efficiency increase of up to 0.2%. (b) The nonaxisymmetric shaping of the labyrinth interaction flow path aims at the secondary flow control in downstream blade rows. This approach might contribute in the same magnitude of order as reduction in the mixing losses.
[DOI: 10.1115/1.2218571]

Introduction

Labyrinth leakage flow in shrouded turbines is looked upon as an inherently detrimental effect and something which the designer cannot avoid. One design recommendation is to minimize the leakage flow through designing better labyrinth seals and to reduce the gap widths as much as possible. If heat transfer is an issue as in a gas turbine the gap must allow enough leakage mass flow in order to cool the turbine shrouds. The inlet to a labyrinth and the exit including the leakage jet alter the flow field in turbine end wall regions. This is of special significance in low aspect ratio turbine stages where secondary flows are strong. The labyrinth seal can be optimized for itself including mechanical limits and through flow coefficients.

The subject of cavity interactions in turbines was initially addressed by Denton and Johnson [1]. However, it is only in recent years that this subject attracted the attention of the turbomachinery research community. Peters et al. [2] examined the effect of gap size on the steady interaction between the leakage flow and the secondary flow field of a subsequent stator in a 1.5 stage, shrouded axial turbine. Hunter and Manwaring [3] reported about two extra vortices generated in a downstream stator blade row. Wallis et al. [4] observed that strong interactions are present in open cavities of shrouded turbine blades. The following blade rows were found to receive the tip flow at a negative incidence. Cao et al. [5] report about an unsteady, incompressible flow phenomenon affecting the interaction between the rim seal and main annulus flows and not being related to the blade passing frequency. Anker and Mayer [6] numerically investigated the leakage interaction with the main flow and found that the tip leakage flow is not uniform in the pitch-wise direction. Schlienger et al. [7] changed the geometry of the labyrinth exit cavities by introducing inserts and compared the effects on the main flow as well as on the efficiency. These studies have focused mainly on the interaction occurring in the main flow and following blade passages.

However, as the origins of these interactions are open cavities, an increased emphasis should be placed on the associated steady and unsteady flow interactions within these cavities. From these considerations the question arises: Is there any potential in improving the overall performance of low aspect ratio, shrouded turbines by looking at the combined system of main flow duct and labyrinth seal? In that respect, the present publication attempts to conclusively summarize and complete the work which already has been published in [8,9]. It is the aim of this publication to give an overview of labyrinth interaction effects occurring in shrouded turbines with large inlet and exit cavities. Additionally, all open cavities are treated in a systematic way and effects on the main flow are discussed and quantified. Based on the detailed flow understanding, which was experimentally gained in a two stage, shrouded, low speed turbine, new design features are derived for a range of open cavities. With this step, design modifications are proposed, which actually make use of the labyrinth interaction flows.

Test Rig, Measurement Technology, and Data Set

The cavity interaction flow was investigated in the two-stage low speed axial turbine "LISA." The test rig is described in detail in Sell et al. [10]. The main characteristics of the turbine are summarized in Table 1.

The constant annulus of the turbine and the four blade rows are depicted in Fig. 1. The stepped shrouds on the blades together with three sealing fins form the labyrinth seal. The geometry under investigation is similar to steam turbine applications, where large inlet and exit cavities allow for axial displacement of the rotor shaft due to thermal expansion of the rotor. Consequently, the blade profiles are of a medium loaded type with 50% reaction and leaned stator blades. The cylindrical coordinate system used in this publication is indicated in Fig. 1. The results are presented looking upstream as the observer indicates. The cavities are numbered for an easier identification in later discussions.

The measurement technology applied was a miniature five-hole probe of 0.9 mm head diameter and a virtual four sensor probe of 0.84 mm head diameter. The accuracy of the five-hole probe readings is discussed in detail in [11]. The corresponding error bars are

Contributed by the International Gas Turbine Institute (IGTI) of ASME for publication in the JOURNAL OF TURBOMACHINERY. Manuscript received October 1, 2003; final manuscript received March 1, 2004. IGTI Review Chair: A. J. Strazisar. Paper presented at the International Gas Turbine and Aeroengine Congress and Exhibition, Vienna, Austria, June 13–17, 2004. Paper No. 2004-GT-53797.

Table 1 Main characteristics of the test turbine

Pressure ratio	1.32	Mass flow	9.86 kg/s
Max power	400 kW	Turbine speed	2700 rpm
T_{inlet}	40 °C	p_{exit}	Ambient
Mach	0.1–0.4	$Re_{C_{ax}}$	10^5
n (rotor/stator)	42	Tip diameter	800 mm
Blade passing	1890 Hz	Blade aspect ratio	1.8

given in the diagrams. In [12] the virtual four sensor probe is described in detail. The advantages of this measurement technology are:

- (1) Very small head, minimizing blockage.
- (2) Three-dimensional flow vector.
- (3) Unsteady total and static pressure field.
- (4) Temporal resolution of the flow field up to 25 kHz.

The results gained with the five-hole probe are considered to be the time averaged picture. A comparison to the virtual four sensor probe showed that this is a justifiable assumption ([12]).

A seal gap variation was performed covering two aspects:

- (a) The first gap variation of 1% blade height is close to the range found in real applications and a realistic flow field in terms of leakage jet strength and mixing can be expected.
- (b) As a second case, a smaller gap width of 0.3% blade height was chosen to investigate the pure main flow to cavity interaction in a more controlled approach.

The experiments were performed at a rotational speed of 2700 rpm and a mass flow of 9.86 kg/s. In real steam turbines the fluid dynamic conditions are $Re=3 \times 10^6$ and $M=0.3$ with a suction peak velocity of around $M=0.8$. Therefore, compressibility as well as viscous effects are not fully modeled in this turbine. How-

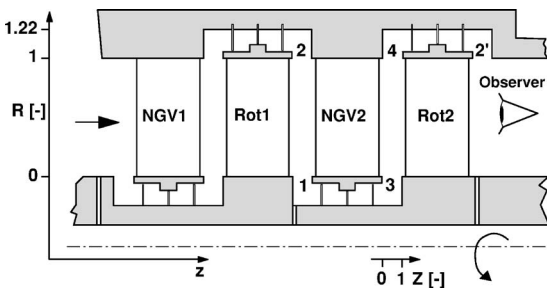


Fig. 1 Meridional cut of the test section

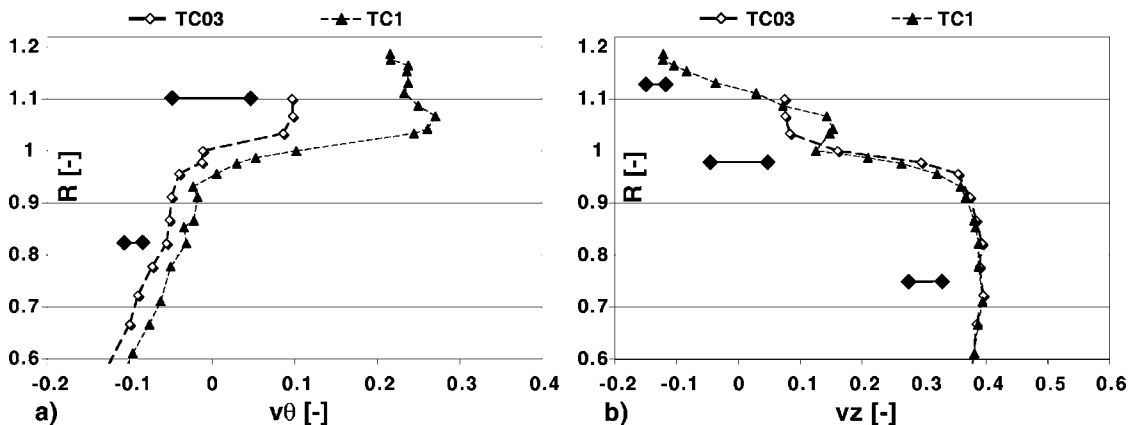


Fig. 2 Pitch-wise mass averaged velocity profiles, cavity 2, Z=0.5: (a) tangential, (b) axial

Table 2 Number of axial measurement planes: 1+1, 1 plane time averaged, 1 plane time resolved

Cavity	1	2	3	4	2'
1% gap	...	1+1	1+0	1+1	1+1
0.3% gap	...	1+1	1+1	6+5	1+1

ever, as the velocity triangles and reduced frequencies match to an actual stage, unsteady effects like vortex or potential field interactions are comparable.

In Table 2 the number of axial measurement planes in each cavity measured with the five-hole probe (time averaged) and measured with the virtual four sensor probe (time resolved) are listed. Most cavities are resolved with one measurement plane containing roughly 350 measurement points. The single plane was positioned in mid-axial gap position ($Z=0.5$). Cavity 4 was resolved with six time averaged and five time resolved measurement planes in the 0.3% gap case having an average spacing of $\Delta Z=0.15$.

Experimental Results and Discussion

Cavity 2 (Outlet, Tip)

Pitch-Wise Mass Averaged Results. First, a short comparison between the velocity fields of the 0.3% and 1% gap case of the seal gap variation is given in Fig. 2. The diagram shows the pitch-wise mass averaged tangential and axial velocity components. The black bars indicate the errors of the five-hole probe measurement chain. The error bars vary with radial height, since the error depends on the flow angle and the Mach number. For the 0.3% gap case the influence of the leakage jet onto the flow field at this location is negligible. The weak jet mixes out quickly downstream of the last seal and is not detected in the velocity profiles. In contrast, the leakage jet in the 1% gap case alters considerably the flow field due to its stronger mass and momentum flux. The leakage fluid can be localized in a radial band from $R=1.03$ to $R=1.07$. For further investigations in this section the authors concentrate on the 1% gap case, where mixing and interaction flows are more realistic than in the 0.3% gap case.

Rotor Relative, Time Averaged Results. The unsteady data sets taken in cavity 2 are postprocessed to the time-averaged picture in the relative frame of reference. The static pressure (3), the relative Mach number (4), and the radial velocity component (5) were chosen for display and discussion. The arrows indicate the sense of rotation of the relative coordinate system. The curved dashed line indicates the tip radius of the turbine blades. The shroud trailing edge reaches from $R=1$ to $R=1.06$. The discussions of the results within this section happen in the relative frame, if not

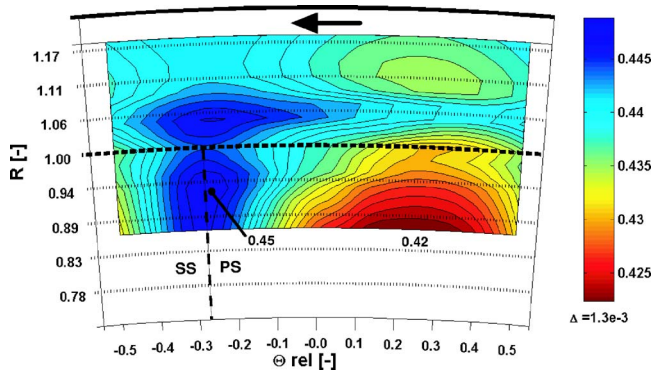


Fig. 3 Nondimensional static pressure C_{p_s} time averaged, rotor relative frame, $Z=0.5$

stated otherwise.

The static pressure distribution (Fig. 3) reveals the trailing edge position of the rotor blade at $\Theta_{rel}=-0.3$ (dashed line), where a high static pressure is induced. The circumferential pressure variation from high to low pressure at $\Theta_{rel}=0.3$ in the main flow region is also seen in the cavity. A stripe of higher static pressure at the radial position of the leakage jet ($R=1.06$) is found. The circumferential variation at $R=1.06$ is such that a low pressure region occurs at $\Theta_{rel}=0.38$. In addition, the level of static pressure within the cavity is on average $\Delta C_{p_s}=0.01$ higher than in the main flow. The circumferential static pressure distribution is imposed onto the cavity flow by the blade to blade pressure field.

The M_{rel} distribution (Fig. 4) shows the rotor wake at $\Theta_{rel}=0.05$ (dash-dotted line). The wake is convected into tangential direction by $\Delta\Theta_{rel}=0.35$ from the location of the trailing edge. On the pressure side of the wake, a higher M_{rel} is detected than on the suction side. Assuming a constant relative total pressure of the rotor exit flow, this effect is induced by the static pressure field.

Closer to the tip radius the wake becomes wider. A band of lower M_{rel} is found between $R=1.03$ and $R=1.07$, which corresponds to the leakage jet position observed in Fig. 2. In a region having its center at $\Theta_{rel}=0.2$ and $R=1.05$, M_{rel} reaches a local minimum of 0.24. The relative total pressure in the cavity is set up by the leakage jet and distributed such that the local minimum in velocity is found on the pressure side of the rotor wake. For this circumferential distribution of the leakage fluid two reasons can be provided: first, the momentum and kinetic energy distribution of the leakage jet at the exit of the last seal and, second, the static pressure field set up by the flow field in the main annulus including the trailing edge pressure field.

Discussing the radial velocity component given in Fig. 5, additional details of the leakage interaction are found. The rotor wake

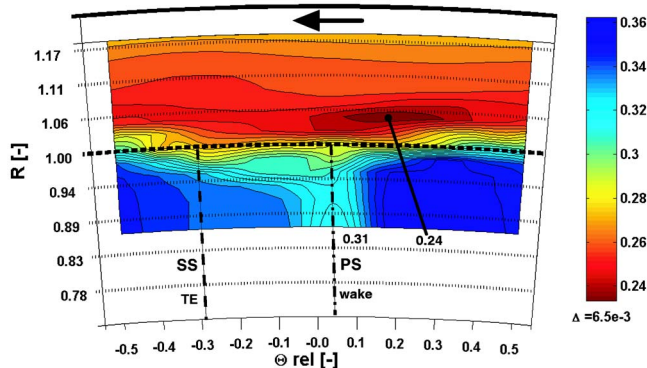


Fig. 4 Relative Mach number M_{rel} time averaged, rotor relative frame; $Z=0.5$

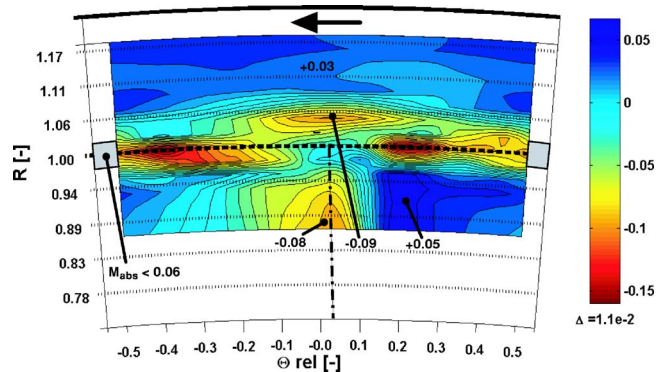


Fig. 5 Nondimensional radial velocity component, time averaged, rotor relative frame, $Z=0.5$

is indicated with the dashed line. The regions of large negative radial velocities $v_r=-0.15$ (red) are not considered for discussion. The reason for this is the fact that the error in the results for the virtual four sensor probe rapidly rises for absolute Mach numbers lower than 0.06. The gray shaded symbols at $R=1$ indicate a band of radial positions where the absolute Mach number falls from 0.1 to below 0.06. This deficit of absolute velocity corresponds to the wake of the shroud. The radial velocity is negative within the region of the leakage jet ($R=1.06$) having a minimum radial velocity of $v_r=-0.09$ at the circumferential position of the wake. This value is of the same order of magnitude as the radial velocity within the wake itself ($v_r=-0.08$). The leakage fluid moves out of the cavity mainly below the wake position, filling up the area of lower relative kinetic energy of the wake.

Leakage to Main Flow Interaction. The basic components of the leakage jet to main flow interaction found in the 1% gap case in cavity 2 comprise three points:

- (1) Leakage fluid migrates into the rotor wake causing the leakage streamlines to contract into the wake area. The radial migration of the leakage fluid leads to a broadening of the wake in the vicinity of the blade tip. The wake seems to attract low kinetic energy fluid.
- (2) The potential field of the rotor trailing edge divides the leakage sheet into distinct jets. Figure 6(a) shows the time averaged relative velocity triangles within the relative frame of reference for the first rotor exit flow field (cavity 2). It represents the velocity vectors found with two cuts in 4, one at $R=0.91$ and the other at $R=1.06$. The upper vectors represent the leakage jet ($R=1.06$) and the lower one the main flow at $R=0.91$. Note that the base of the velocity vector is representing the location of the circumferential coordinate. The arrow represents 100% of the shroud rim speed. The circles point out the base of velocity vectors, which are facing the trailing edge position of the rotor $\Theta_{rel}=-0.25$. The leakage mass flow is redistributed from a homogeneous distribution within the last gap. A maximum of leakage mass flow is found in the mid position between the trailing edges where it forms a distinct jet (see the dotted ellipse). The main flow is much less affected by the trailing edge pressure field than the leakage jet. The main flow vectors reveal the wake of the rotor blade.
- (3) The potential field of the stator leading edge three-dimensionally redistributes the flow field in the absolute frame of reference. This effect is visualized in Fig. 6(b), which presents the circumferential distribution of the absolute velocity triangles in the stator frame of reference for the 1% gap case. The diagram depicts the velocity vectors of the leakage fluid in the upper part and the velocity vectors of the main flow at $R=0.9$ in the lower part. The ve-

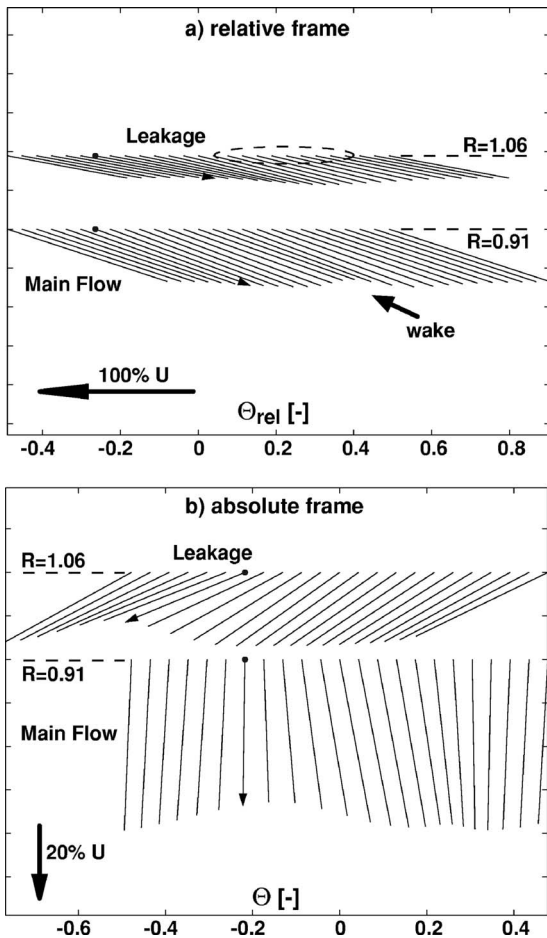


Fig. 6 Time averaged velocity triangles, cavity 2: (a) relative frame, (b) absolute frame

locity arrow represents 20% of the shroud rotational speed. The leading edge position of the stator is obvious in the downstream flow field of the first rotor (cavity 2), where it causes a deviation of streamlines. The circles point out the

base of velocity vectors, which are facing the leading edge position of the stator at $\Theta_{rel} = -0.22$. Downstream of the second rotor (cavity 2') this effect is not present and the velocity vectors of the leakage jet are constant around the circumference (not shown in a diagram).

These observations are brought together in a descriptive flow model given in Fig. 7(a). The arrows indicate the rotor passage vortex, the radial migration within the wake, and the tangential redistribution of the leakage mass flow (red) due to the rotor trailing edge pressure field. The gray shaded area corresponds to the higher leakage mass flow and the blue ellipse marks the area of the radial movement of the leakage fluid out of the cavity into the wake.

Mixing Calculation. At this stage of investigation it is of interest to know the losses generated by the leakage jet mixing with the main flow. Since the mixing is a three-dimensional process, the authors propose a two-step mixing approach in order to capture pitch-periodic effects. From the experimental results, it is known that the radial movement of the leakage fluid (Fig. 5) out of the cavity occurs prior to the full mixing of the two streams. In this radial movement different flow qualities do interfere due to the fact that the flow is nonaxisymmetric (wake, leakage mass distribution). Therefore, the mixing process is modeled in two steps as indicated in Figs. 7(b)–7(d):

- (1) The idealized flow field shown in Fig. 7(b) is describing the situation depicted in Fig. 7(a). Two areas represent the leakage and main flow each having its proper tangential variation in velocity triangles. The first mixing step is performed under constant area for each of the 20 circumferential sections of the blade pitch (Figs. 7(b) and 7(c)).
- (2) The second step is performed mixing all 20 stripes to the final mixed out situation (Figs. 7(c) and 7(d)).

The boundary conditions for this mixing calculation are given in Table 3. The inner radius of the mixing domain R_i was set to 0.72 such that the loss core of the stator is covered. This implies that the mixing of the leakage jet with the main flow will be restricted to the end wall region rather than mixing with fluid at the hub. The outer radius R_o was adjusted to the leakage to main mass flow ratio. From the measurement with FRAP probes one

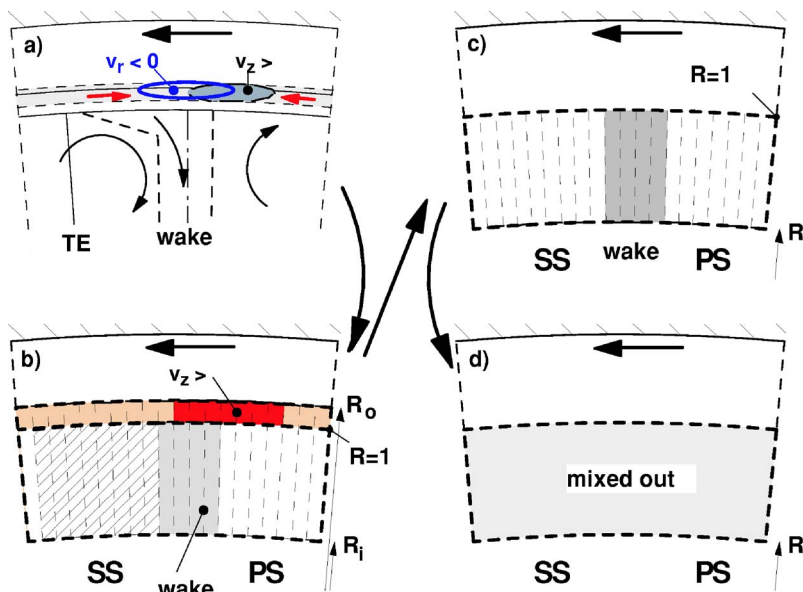


Fig. 7 (a) Rotor relative descriptive flow model, (b)–(d) two-step mixing calculation of leakage and main flow

Table 3 Boundary conditions for mixing calculation

$R_0 - R$ [-]	T_{rel}^o [°C]	p [kPa]	\dot{m}_L/\dot{m} [%]
0.028	Jet: 34.7 Main: 33.3	11.0	1.39

also gains the time averaged total temperature of main and cavity flow. The leakage jet was found to have a 1.4°C higher relative total temperature than the main flow.

The mixing losses are expressed in terms of entropy rise as calculated with the entropy equation

$$\Delta s = c_p \ln \frac{\overline{T}_0}{T_2} - R \ln \frac{\overline{p}_0}{p_2} \quad (1)$$

The indices refer to the stagnation values of temperature and pressure at the inlet and exit of the stage. The values of entropy are nondimensionalized using the stage losses as derived from the performance measurements (see Table 4). The mixing of the leakage jet downstream of the first stage generated 6.7% of the stage losses, where on average 22% of the loss is contributed by the mixing of different total temperature streams.

Cavity 3 (Outlet, Hub). In Fig. 8 the pitch-wise mass averaged results are presented and a comparison of the 0.3% and 1% gap case is given. The velocity components are made nondimensional with the rotor hub speed. The total pressure of the cavity flow

Table 4 Mixing losses of cavity 2, contribution of temperature term to entropy generation

	P_{mix} [% stage loss]	$\Delta S_T/\Delta S$ [%]
1% gap	6.7	22

depends strongly on the gap width. A larger gap decreases the total pressure which is in conjunction with a lower tangential velocity component. A reason for this could be that the higher leakage mass flow in the 1% gap case has not fully adjusted to the circumferential speed of the rotor hub cavities. In the 0.3% gap case the tangential velocity in the cavity is much closer to the hub velocity. The axial velocity component (Fig. 8(b)) shows a mass deficit around $R=0.05$ in the 1% gap case and a higher axial velocity at $R=-0.08$. The first is caused by the higher mass flow being sucked into the inlet cavity, the latter is due to the stronger leakage mass flow. The point of zero through flow $v_z=0$ is located at $R=-0.12$.

Surprisingly, the radial velocity components (Fig. 8(d)) show mostly negative values. The radial migration of flow under the radial static pressure gradient is one explanation for the main flow region. However, the leakage mass flow was expected to show on average positive radial velocity components since the leakage mass flow has to leave the cavity at some point. In the circumferential mass averaged diagram this seems to happen further downstream, e.g., at $Z=0.8$. A stronger outflow between $Z=0.8$ and 1 would also explain the difference in radial velocity component at $R=0.05$ between the two gap cases. The main flow streamlines at this point ($Z=0.5, R=0.05$) would see a greater blockage at the rotor hub, causing the streamlines to bend into the main flow again ($\Delta v_r > 0$).

The velocity triangles of the leakage ($R=-0.08$) and the main flow ($R=0.2$) for both gaps are compared in Fig. 9. From this, the rotor hub region can expect a negative incidence around $\Delta\beta = -70$ deg. This large value might decrease, if the leakage flow passes the exit corner of the cavity, where the fluid is accelerated and deviated into stream-wise direction.

Figure 10 presents the total pressure and the radial velocity component distribution at $Z=0.5$ of the 1% gap case. The thick dashed line represents the hub radius of the blades. The thin

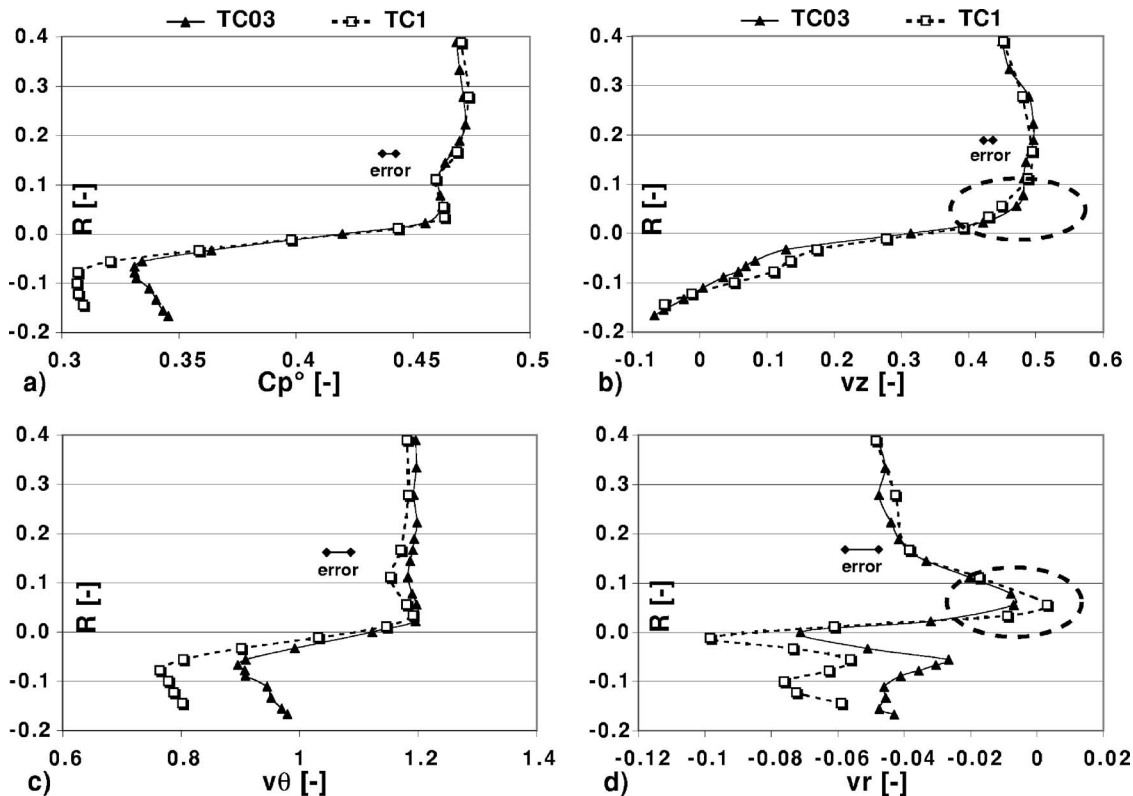


Fig. 8 Pitch-wise mass-averaged, $Z=0.5$: (a) total pressure, (b) axial, (c) tangential, (d) radial velocity components

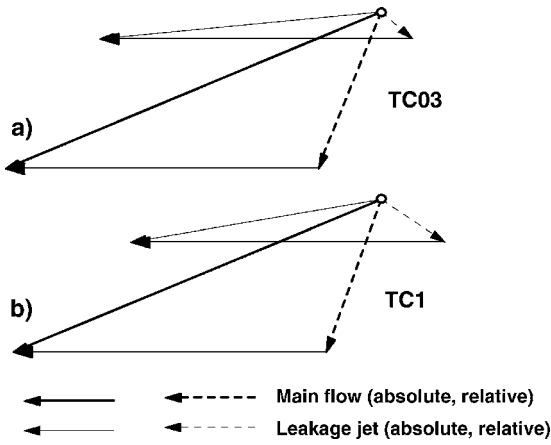


Fig. 9 Pitch-wise mass-averaged velocity triangles, $Z=0.5$: (a) 0.3% gap, (b) 1% gap

dashed lines are indicating the stator trailing edges which also go along with a high static pressure region. The dash dotted line highlights the position of the wake. The loss core is small since the incoming boundary layer is sucked away at the hub inlet cavity. The wavy flow structure between the main and the cavity flow is showing a distinct inflow jet on the pressure side of the wake similar to what was found for cavity 4 in [9]. Below the wake position ($\Theta=0.25$) the radial velocity becomes positive. This is also the region where most of the leakage flow will leave the

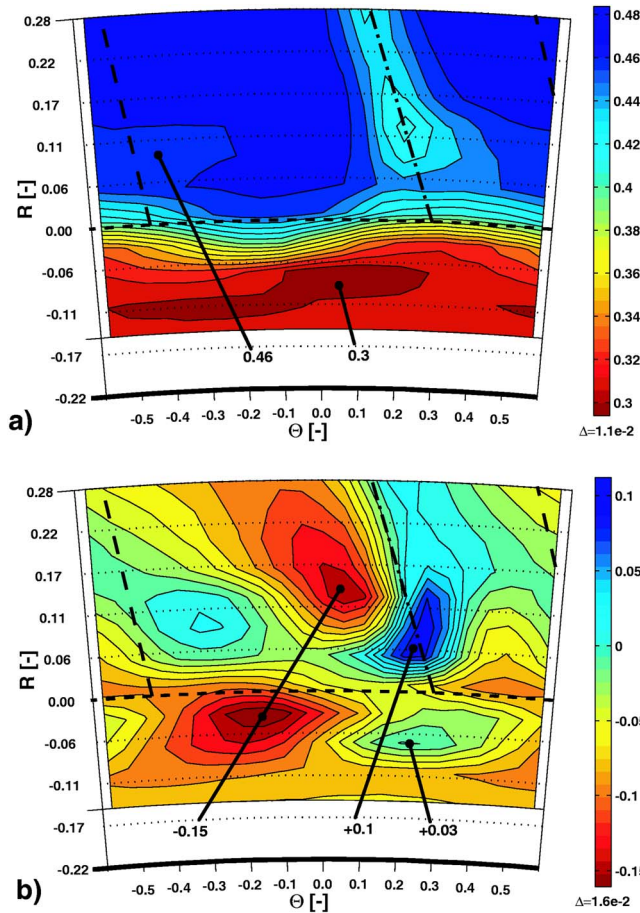


Fig. 10 Downstream stator 2, 1% gap case, $Z=0.5$: (a) total pressure, (b) radial velocity component

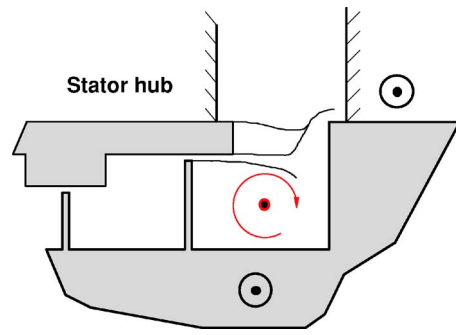


Fig. 11 Flow model for cavity 3

cavity further downstream.

From these observations a short descriptive flow model can be given for this cavity (Fig. 11). The thin lines indicate dividing stream lines. The static pressure field set up by the high swirl and the stator trailing edges is expanding into the cavity. This has two consequences:

- (1) The leakage flow is rather pushed into the cavity rolling up into a toroidal vortex, than moving out of the cavity immediately at $Z=0.1$. The outflow happens further downstream around $Z=0.9$.
- (2) The three-dimensional pressure field redistributes the leakage mass flow such that most of it will leave the cavity at a certain circumferential position relative to the stator leading edge. Due to the convection of the wake into tangential direction both locations (wake and outflow) might coincide (e.g., at $\Theta=0$).

Cavity 4 (Inlet, Tip). In an earlier publication, Pfau et al. [9] described the vortical flow structure in the inlet cavity (cavity 4) as in- and outflows set up by the stator flow field. A toroidal vortex was observed moving at high tangential velocity (83% of rotor speed). This toroidal vortex was discovered to be subject to unsteady vortex stretching. In this publication further details and quantification of the flow are presented.

Results on the Interface Surface. The interface surface between the cavity and the main flow is defined as a cylindrical surface with $R=1$. In the absolute frame of reference the radial velocity distribution shows the location of in- and outflows set up by the stator flow field as presented in Fig. 12(a). At the axial position $Z=0.5$ a comparison between the two gap cases is given in Fig.

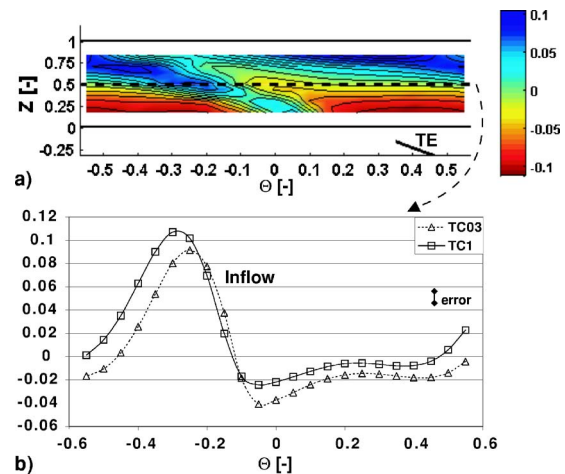


Fig. 12 Radial velocity component, absolute frame: (a) interface surface, $R=1$, 0.3% gap, (b) $Z=0.5$, 0.3% and 1% gap

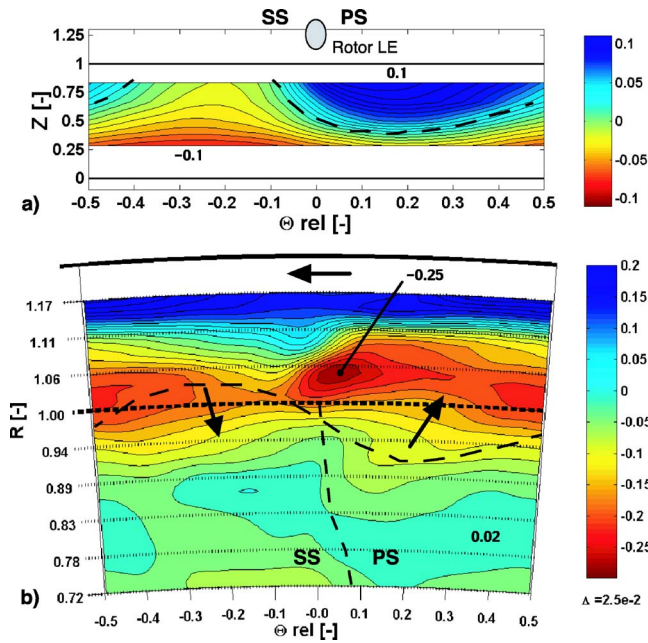


Fig. 13 Relative frame: (a) Radial velocity component, 0.3% gap, $R=1$, (b) relative stream-wise vorticity, $Z=0.83$

12(b). The shape of the circumferential distribution of the radial velocity component is the same, but the level is shifted according to the bigger leakage mass flow being sucked into the cavity for the 1% gap case. The inflow region with positive radial velocity component is obvious. The corresponding fluid stems from the pressure side corner of the stator passage, as described in [9].

Within the relative frame the radial velocity distribution given in Fig. 13(a) shows the upstream effect of the rotor passage. The isoline of zero radial velocity is indicated with a dashed line. On the pressure side of the rotor passage fluid is pushed into the cavity, while it is sucked out on the suction side. This interaction process is an additional contributor to the torque balance of the cavity, which will be discussed in the following section. Furthermore, it alters the inflow condition to the rotor end wall region considerably. For the discussion of this effect Fig. 13(b) shows the relative stream-wise vorticity distribution time averaged in the rotor relative frame of reference. The dashed line indicates the zero radial velocity isoline. The arrows indicate that negative stream-wise vorticity is sucked into the rotor passage on the suction side. This fluid has the same rotational direction as the rotor passage vortex which develops further downstream in the passage.

Mass and Momentum Exchange

Time averaged (absolute frame). The mass and momentum exchange due to the interaction of the main flow with the open inlet cavity is investigated using the control volume as shown in Fig. 14(a) and an integration tool. The integration tool uses linear interpolation within the measurement grid. Each time step is evaluated in a quasisteady way. Nonslip conditions at the stationary and rotating walls are applied. The region between the nearest measurement point to the point on the wall is linearly interpolated. The integration can be performed on surfaces of constant radii, constant axial, or circumferential position. In circumferential direction, pitch-periodic conditions are assumed. The boundary conditions on the inlet and exit axial plane $Z=0$ and $Z=1$ are set to the measurement values of the closest measurement plane.

The outer surface at $R=1$ represents the interface between main and cavity flow. The inner surface was chosen to $R=0.91$. At this radial location the area integration of constant radius delivers a net radial mass flow of approximately 0. For $R>0.91$ this integration

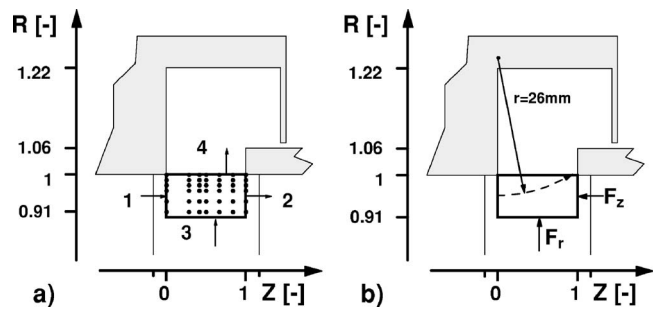


Fig. 14 Control volume for mass and momentum integration: (a) measurement grid, (b) external forces on control volume F_r , F_z ; radius of average streamline curvature

becomes positive, for $R<0.91$ negative. Therefore, $R=0.91$ is interpreted as a dividing stream surface: Below $R=0.91$, the negative radial migration of the main flow dominates, above $R=0.91$ the flow field is affected by sucking mass into the cavity.

The results of the integration are given in Table 5 representing the full annulus. Fluxes out of the control volume are counted positive and external forces on the control volume are calculated. In tangential direction the momentum flux is expressed as torque.

Considering first the sum of mass flows and fluxes in the last row of Table 5, continuity is preserved within 11 g/s, which is 0.1% of the main mass flow. The sum of the momentum fluxes is positive in radial and negative in axial direction. Sucking mass flow into the cavity reduces the axial momentum in the end wall region, since some of the incoming axial momentum is transformed into radial momentum. In tangential direction, the sum is close to 0, since no external forces act in this direction. The components of the external force acting on the control volume are depicted in Fig. 14(b).

The mass flow passing through the control volume amounts to 6% of the main mass flow. The assumption $\dot{m}_3=0$ is met to within 0.02% of the main mass flow. The net mass flow at surface 4 compares well to the leakage mass flow, which was evaluated to 37 g/s. Associated to the inflow into the cavity at surface 4 is the transport of a torque of 1.8 Nm.

The local radial pressure gradient across this control volume is not sufficient to keep the flow on a constant radius. Streamlines from the stator pressure side corner enter the cavity. This effect arises from the presence of a sudden area increase due to the cavity and from the sucking of the leakage mass flow. The radial equilibrium of forces acting on a circular motion is given by

$$v_z \frac{\partial v_z}{\partial z} \sin \gamma + \frac{v_z^2}{r_z} \cos \gamma - \frac{v_\theta^2}{r} = -\frac{1}{\rho} \frac{\partial p}{\partial r} + \frac{F_r}{\rho V} \quad (2)$$

where r_z denotes the radius of the streamline in the meridian plane. The first term describes the radial acceleration along the streamline. The second term is the radial component of the centripetal acceleration due to the meridian curvature. The third term on the left-hand side represents the centripetal acceleration directed radially inward due to the main swirling flow. These three terms are balanced by the radial pressure gradient and the radial

Table 5 Control volume integration according to Fig. 14(a): mass flow and momentum fluxes on the full annulus

Surface i	\dot{m}_i [g/s]	F_{ir} [N]	T_i [Nm]	F_{iz} [N]
1 (in)	606	0.5	-24.2	-17.1
2 (out)	-562	1.8	22.3	14.2
3 (in)	2	0.4	-0.2	-0.2
4 (out)	-35	0.4	1.8	0.6
Sum	11	3.1	-0.3	-2.4

Table 6 Mass and momentum fluxes across surface 4, absolute frame

Surface i	\dot{m}_i [g/s]	F_{ir} [N]	T_i [Nm]	F_{iz} [N]
4 (in, $v_r > 0$)	127	0.9	5.1	1.5
4 (out, $v_r < 0$)	-92	-0.5	-3.3	-0.9
Sum	35	0.4	1.8	0.6

external force. In this case, Eq. (2) can be simplified with the help of the experimentally based assumption that the pitch angle of the initial streamlines in surface 1 of Fig. 14(a) is approximately zero which leads to

$$\frac{v_z^2 v_\theta^2}{r_z r} = -\frac{1}{\rho} \frac{\partial p}{\partial r} + \frac{F_r}{\rho V_{CV}} \quad (3)$$

The unknown in this equation is r_z . All other terms can be derived out of the measurement volume. The second term on the left-hand side is evaluated in taking the arithmetic average of all values within the control volume according to

$$\frac{v_\theta^2}{r} = \frac{\overline{v_{\theta ijk}^2}}{r_{ijk}} \quad (4)$$

A representative radial pressure gradient is found in taking the pressure difference of each opposing pair of grid points, which lay on surfaces 3 and 4. These local pressure differences are arithmetically averaged. The external radial force is taken from Table 5. An average v_z on surface 1 can be given to 19% of shroud rim speed. From this approach a representative streamline with an average meridian radius of $r_z = 26$ mm is calculated. The streamline is included in Fig. 14(b) with a dotted circular arc starting at mid-radial height of surface 1 with an assumed pitch angle $\gamma = 0$. The inflow of surface 1 connects well to the area around $Z = 0.8$ of surface 4, where most of the inflow to the cavity happens (see also Fig. 12(a)).

The axial component of the external force F_z (Table 5) is the result of a static pressure increase across the cavity. To verify this assumption a pressure force integration was performed taking the measured static pressure at surfaces 1 and 2. The force calculated with the pressure difference becomes -2.6 N, which compares well to the control volume integration. Across the cavity opening a positive axial pressure gradient is observed. The same procedure applied to the main flow region ($R < 0.91$) results in a negative axial pressure gradient as expected.

Additional insight could be gained by observing the quantities associated to the in- and outflows across surface 4, which are summarized in Table 6. As much as four times of the leakage mass flow enters the cavity and convects up to 5 Nm of torque, 0.9 N of radial momentum flux, and 1.5 N of axial momentum flux. The outflow of roughly three times the leakage mass flow conveys less momentum in all three components. However, the major contribution to the radial and axial momentum balance of the control volume are found in surfaces 1 and 2.

Time averaged (rotor relative frame). The associated fluxes to the in- and outflow generated by the rotor pressure field are discussed in this section. To do so, the surface integration of surface 4 in Fig. 14 was performed in the relative frame of reference. The radial velocity distribution of this surface is presented in Fig. 13(a). In comparison to Fig. 12(a), the results are restricted to five axial positions, which reduces the area covered by experimental results. The integration results are shown in Table 7. The mass flow integration compares well to the results in Table 6 because the time averaged radial velocity components were adjusted to the five-hole probe results. The radial component of momentum fluxes is larger than in the stator relative flow field. The axial component of the momentum fluxes compares well to the results

Table 7 Mass and momentum fluxes across surface 4, rotor relative

Surface i	\dot{m}_i [g/s]	F_{ir} [N]	T_i [Nm]	F_{iz} [N]
4 (in, $v_r > 0$)	148	1.6	1.1	1.4
4 (out, $v_r < 0$)	-110	-0.6	-1.3	-0.9
Sum	38	1.0	-0.2	0.5

in the absolute frame of reference. The important result here is that the rotor in time average extracts torque from the cavity, since the sum of in- and outflows is negative.

Systematic Classification of Open Cavities

Characteristics of Open Cavities. There are three characteristics in which the open cavities differ (see also Table 8):

(I) *The strength of the radial pressure gradient at the interface surface due to the swirling main flow:* Downstream of the stator the swirl angle is constantly high inducing a much stronger radial pressure gradient ($dCp_s/dR = 0.02$) than downstream of the rotor ($dCp_s/dR = 0.004$). The exit flow of the rotor depends on the power extraction in which the stage is working. In the case of medium loaded stages the exit swirl of the rotor is small.

(II) *The location at hub or tip:* Radial pressure gradients are pointing either out of the cavity as is the case at the tip or pointing into the cavity as at the hub. Low kinetic energy fluid migrates on lower radii according to the pressure gradient than fluid of higher kinetic energy. Therefore, the leakage fluid in cavity 3 under the influence of the radial pressure gradient set up in the main flow region moves closer to the hub with negative radial velocity, thus forming the toroidal vortex there. The center of the vortex is found at $R = -0.12$. At the tip, the low kinetic energy fluid within the cavity is sucked out of the cavity, such that the center of the toroidal vortex in cavity 4 moves toward lower radii ($R = 1.06$) and the vortical flow is observed at the interface surface ($R = 1$).

(III) *The leakage jet:* The leakage jet in the exit cavities adds fluxes of axial and tangential momentum to the cavity flow. In addition, the mixing of the jet is a loss production mechanism. The leakage mass flow does no work to the rotor. This causes a higher total temperature of the leakage flow than the main flow downstream of the rotor. Downstream of the stator the total temperature of both fluxes is the same. Within the inlet cavities no jet is present, but end wall fluid is sucked into the labyrinth seal. Thus, the inlet cavity acts as a sink of axial and tangential momentum.

Table 8 Characteristics of open cavities in turbines

No.	Swirl I	Position II	Jet III	Incidence a)	Loss production b)
1	-	Hub	-	$\Delta\alpha = 0$ deg sucking	Sucking of BL at hub, smaller hub loss core and secondary flows in rotor passage
2		Tip	$T_j^o > T_m^o$	$\Delta\alpha = -30$ deg	Mixing of the jet with cavity and main flow Jet increases. BL-thickness
3	++	Hub	$T_j^o = T_m^o$	$\Delta\beta = -70$ deg	Mixing of the jet with cavity and main flow Secondary flow development in rotor passage
4	++	Tip	-	$\Delta\beta = -7$ deg sucking	Vortex stretching, wall friction in cavity Secondary flow development in rotor

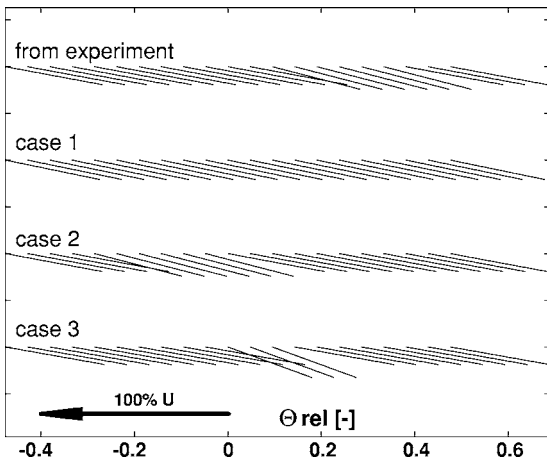


Fig. 15 Rotor relative descriptive flow model and two-step mixing calculation of leakage and main flow

Influence on Main Flow and Performance. Each of the open cavities differs in their influence on the main flow and the performance of the machine. The effects discussed here are the change of incidence and the loss production mechanisms induced by the corresponding cavity (Table 8).

(a) *Incidence angle to the end wall regions of downstream blade rows:* The leakage jet in cavities 2 and 3 causes a negative incidence due to the mismatch of the velocity triangles. At the inlet to the downstream blade row the incidence angles at the end wall regions are of the order of -30 deg and -70 deg. Cavity 4 induces negative incidence via sucking of circumferential momentum. Evaluating the flow with the help of a control volume analysis and further modeling the flow predicts an incidence angle of -7 deg for the 1% gap case. Cavity 1 is estimated to induce no incidence since the exit flow of the rotor, which is sucked into the hub labyrinth, has no circumferential momentum.

(b) *Loss production mechanisms:* Sucking of boundary layer fluid at cavity 1 can be beneficial, since a thinner boundary layer enters the stator hub and thus less secondary flow is generated. In cavity 4 the effect of sucking may be less beneficial since the cavity is pressure loaded and interaction mass flows of up to four times the leakage mass flow do leave the cavity again. These interaction outflows then enter into the rotor tip region enhancing the secondary flow development with a sheet of positive stream-wise vorticity at the suction side of the rotor passage (see Fig. 13(b)). In addition cavity 4 contributes to the loss production via vortex stretching and enhanced wall friction due to the toroidal vortex system. In cavities 2 and 3 the leakage jet mixes with the cavity and main flow in addition to generating strong negative incidences to the downstream blade rows.

Design Proposals

In this section the gained flow understanding is used to propose design changes and to quantify a beneficial effect if possible.

Cavity 2. The approach for cavity 2 is to optimize the leakage mixing process. As reported in the previous section, 6.7% of the stage losses are attributable to the mixing. In a further step of investigation the mixing calculation model was used to investigate three cases of leakage mass distribution. The cases are visualized in Fig. 15. The upper distribution of velocity vectors belongs to the experimentally found situation.

Case 1: Homogeneous distribution of velocity vectors.

Case 2: Mirrored at $\Theta_{rel}=0$.

Case 3: Most of the leakage mass flow into the rotor wake.

By varying the leakage vector distribution the leakage mass flow as well as the momentum fluxes were kept constant. From this approach, an improvement of 0.1% in efficiency is predicted

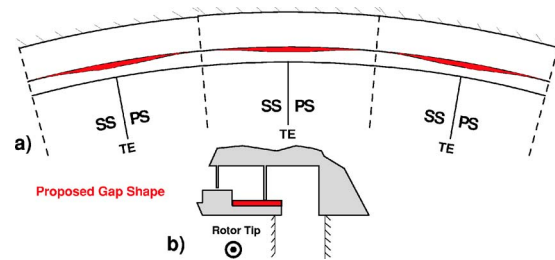


Fig. 16 Nonaxisymmetric shroud design in cavity 2: (a) upstream view of the last sealing gap, (b) side view

for cases 1 and 3 in comparison to the experiment. Case 2 does not show improvements. In case 1, downstream blade rows receive a more homogeneous inflow, which is in accordance to Dawes' comment about design goals in end wall regions [13]. Case 3 seems to be beneficial, since feeding the leakage flow into the wake reduces nonuniformity in the main flow and therefore reduces the mixing contribution in step 2 of the mixing model. Despite the rough assumptions applied to the mixing model, the results do indicate possible improvements.

In order to achieve a leakage jet distribution similar to case 3, a design modification for a nonaxisymmetric shroud contour is proposed, as shown in Fig. 16. The gap variation around the circumference varies between completely closed at mid-pitch and open at the rotor trailing edge position. The gap area is kept the same as in the 1% gap case. The leakage mass flow passing through the seal gap below the trailing edge will end up mixing with the rotor wake, when the leakage fluid leaves the cavity. Thus the leakage flow is used to reduce nonuniformities in the end wall region of the turbine.

The design of the nonaxisymmetric gap depends on the re-entry behavior of the leakage flow. A simple model is proposed to describe the circumferential position of the maximum gap relative to the rotor trailing edge ($\Delta\Theta_{relG}$) as depicted in Fig. 17. The model uses three parameters:

- (1) The characteristic length scale of the problem is the axial gap width of the exit cavity z_{cav} .
- (2) The average relative flow angle of the leakage flow from last seal gap to the re-entry into main flow β_L .
- (3) The relative flow angle of the main flow at the rotor tip β_T .

In addition, the designer has to define the location along the convective path of the wake, where it is desirable to let the leakage flow interact with the wake (wake window). These parameters combine to the nondimensional circumferential position of the maximum gap of

$$\Theta_{relG} = \frac{z_{cav}}{p} (\tan \beta_T - 1.3 \tan \beta_L) \quad (5)$$

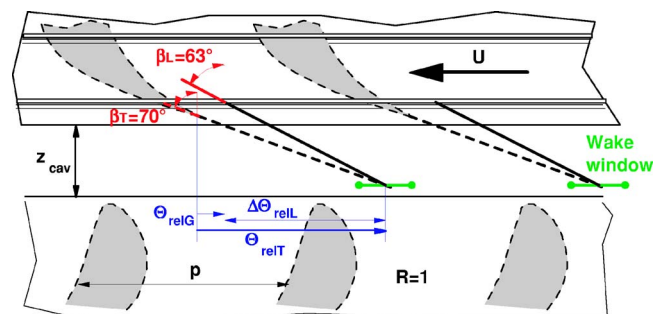


Fig. 17 Simple model for shroud design

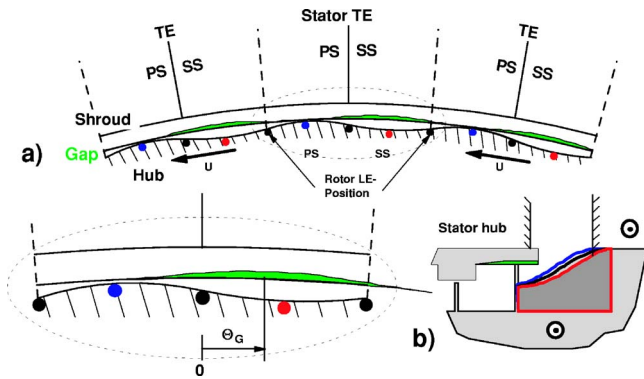


Fig. 18 Nonaxisymmetric shroud and cavity design, cavity 3: (a) upstream view, $Z=0.5$, (b) side view with nonaxisymmetric insert

The local blade pitch is denoted with p . The factor 1.3 describes the geometric fact of this configuration, that the leakage jet starts at a more upstream axial position than the wake (seal gap position versus trailing edge position). For this test case and cavity the position for the maximum gap results in $\Theta_{relG}=0.05$, which is very close to the trailing edge position.

Cavity 3. In cavity 3, the same principal as described above for cavity 2 can be applied. Thus a more uniform flow distribution would be generated at the inlet to the rotor hub and the leakage mixing losses would be reduced. As reported in [7], inserts into the exit cavities were investigated preventing the toroidal vortex to develop and guiding the leakage flow back into the main flow. The upstream effect of the rotor passage onto the leakage flow and distribution on the incoming vorticity field has been shown in the experimental results for cavity 4. In order to control the mixing and the re-entry of the leakage flow at the hub the authors propose to extend the idea of nonaxisymmetric end wall contouring as described, e.g., in [14] or in [15] into the exit cavity and combine it with the nonaxisymmetric design of the shroud trailing edge and last seal gap. The resulting design is depicted in Fig. 18. The gap shape is highlighted in green. The maximum gap is shifted to the suction side of the stator passage. Thus the leakage flow can be expected to reenter into the main duct at the circumferential position of the stator wake.

Using the approach presented for cavity 2, an equation for the hub exit cavity can be given

$$\Theta_G = \frac{z_{cav}}{p} (1.3 \tan \alpha_L - \tan \alpha_H) \quad (6)$$

Taking an average flow angle of the leakage fluid of $\alpha_L = 75$ deg and the swirl angle at the hub $\alpha_H = 67.5$ deg, this results in a circumferential position of the maximum gap of $\Theta_G = 0.8$, relative to the stator trailing edge position. The underlying assumption is that the average flow angle of the leakage α_L remains the same with the inserts. The beneficial effect will be of the same order as in cavity 2, i.e., around 0.1% absolute turbine efficiency.

The nonaxisymmetric insert is designed such that the leakage flow is guided into the rotor passage in a favorable way. The design shifts the incoming leakage fluid onto the suction side of the rotor passage. This aims at two effects:

- (1) The leakage fluid is found on the suction side, thus the secondary flow development in the passage due to the movement of the low kinetic energy fluid in the cross passage pressure gradient is reduced. Wall shear stresses at the end wall due to the development of a new boundary layer could be reduced.
- (2) The distribution of the leakage fluid to the suction side reduces the likelihood of a separation bubble at the pressure

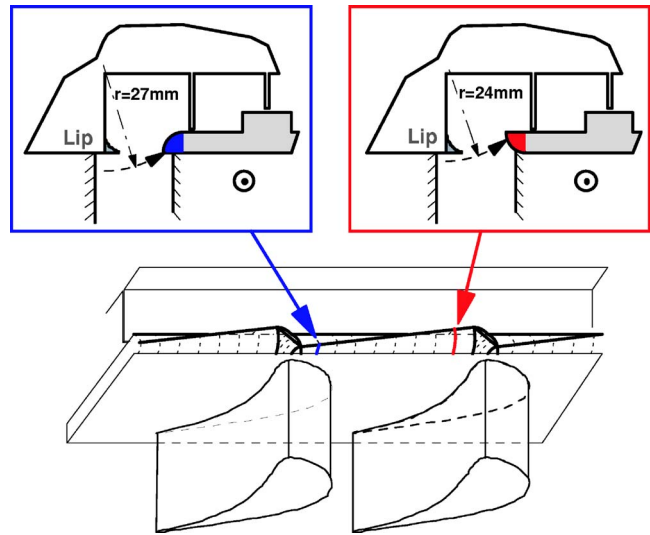


Fig. 19 Shroud leading edge design for reduced rotor passage to cavity flow interaction

side of the rotor leading edge due to the strong negative incidence of the leakage flow. Instead of leakage fluid, a thin boundary layer of main flow fluid is hitting the rotor leading edge at the correct angle of attack.

Cavity 4. The inlet cavity to the rotor tip labyrinth seal is subject to large in- and outflows as described in detail in [9]. Three approaches will be discussed, which are considered to be favorable in terms of loss production and reduction of unsteady interaction and secondary flows.

(1) Nonaxisymmetric end wall contouring in the stator passage is a promising tool to reduce secondary losses as reported in [16]. This approach has the potential to reduce the inflow and outflow due to the end wall curvature. Applied to the inlet cavity this would mean that the end wall on the pressure side would have to be convex. The induced static pressure drop would provide the fluid in the pressure side corner with additional kinetic energy. Thus the fluid particles tend to penetrate less into the cavity. The same target can be followed by introducing a local lean to the stator trailing edge, which would cause a local load increase. The pressure side corner fluid then would experience an additional radial force due to the imposed local static pressure gradient. A larger radius of streamline curvature is resulting from this and less amount of fluid is penetrating into the cavity.

(2) The lip on the stator side of the cavity, as depicted in Fig. 19, is designed to reduce the circumferential wake as found in [9] and to turn the fluid at the edge of the toroidal vortex into axial direction. The static pressure gradients originating from the stator trailing edge and acting on the interaction zone are reduced due to the potential field decay.

(3) The shroud leading edge depicted in Fig. 19 is designed to reduce the interaction flow across the cavity-to-main flow interface. One expected effect would be that the radial velocity distribution as presented in Fig. 13(a) is more homogeneous and the peak radial velocities are reduced. On the pressure side of the rotor passage the shroud leading edge is positioned at a higher radius than on the suction side. The effect of this is that streamlines of a lower curvature are entering on the pressure side. Less fluid is pushed into the cavity at this point. On the suction side, the cavity fluid has to reach lower radii in order to be sucked into the rotor passage. In terms of streamline curvature, more fluid is pushed into the cavity at the suction side than on the pressure side.

The design modification described above with the help of Fig. 19 can be inverted, i.e., it is the goal to enhance the interaction flow such that the inlet stream-wise vorticity distribution as found

in Fig. 13(b) would show a higher value at the suction side to the rotor tip inlet. Consequently, the rotor passage vortex would increase its strength and change position. At first glance, this might not be a beneficial effect. But considering a designer's need to increase the rotor tip passage vortex in order to compensate incoming or downstream vorticity of the opposite sign (vortex interaction), this might be the correct approach.

Conclusions

Detailed flow understanding is the key issue to further push the edge of the aerodynamic performance of state-of-the-art turbines. This paper presented a systematic investigation and description of the influence of large open cavities on the end wall flow region of shrouded axial turbines. This is of particular interest to low aspect ratio, high pressure stages, where secondary flows are significant. From the flow understanding design modifications have been deduced. Based on the quantitative prediction of the beneficial effect for one design modification, an optimum design suggests a potential of 0.2%–0.5% on the overall turbine efficiency. This gain can be made through applying and optimizing all the above-described design modifications. The basic idea is to introduce a new degree of freedom into the shroud and cavity design: the nonaxisymmetric shape. These modifications make use of the nature of the labyrinth interaction flows. Secondary flow development in downstream blade rows can be actively changed and the leakage fluid can be actively distributed. Secondary flow development within the blade rows as well as mixing losses should be optimized with the leakage flow development aiming at better turbine efficiency.

Acknowledgment

The flow measurements in the turbine were supported by the German Federal Ministry of Economy (BMWI) under File Nos. 0327060D and 0327060F. The authors gratefully acknowledge AG Turbo, Alstom Power, and Rolls-Royce Germany for their support and permission to publish this paper.

Nomenclature

r, θ, z	= cylindrical coordinate system
g	= radial gap width in % of blade height
h	= blade height, 90 mm
z_{cav}	= axial cavity width, 15 mm
n	= numbers of blades, 42
f_{blade}	= blade passing frequency
M	= Mach number
p, p^0	= static, total pressure
p	= local blade pitch, $2\pi/42$
P	= mixing loss in % of stage loss
R	= nondimensional radial height $r - r_{\text{Hub}}/r_{\text{Tip}} - r_{\text{Hub}}$
Re	= Reynolds number
s	= specific entropy
T	= blade passing period $1/f_{\text{blade}}$
T, T^0	= static, total temperature
U	= local blade speed
V	= volume
Z	= nondimensional axial distance z/z_{cav}
v	= nondimensional velocity u_{loc}/U
C_p	= nondimensional pressure
	$C_p = p_{\text{local}} - p_{\text{stat,out}}/p_{\text{total,in}} - p_{\text{stat,out}}$
α	= absolute yaw angle
β	= relative flow angle

γ	= pitch angle
Ω	= nondimensional vorticity $\omega/(4\pi f_{\text{blade}})$
Θ	= nondimensional circumferential position θ/p

Indices

G	= maximum gap position
H	= hub
i	= inner
L	= leakage jet
o	= outer
rel	= relative system
r, θ, z	= corresponding components in the coordinate system
T	= tip
0,2	= inlet, exit condition of the turbine

Abbreviations

TC03	= 0.3% seal gap case ($g=0.3\%$)
TC1	= 1% gap case ($g=1\%$)
FRAP	= fast response aerodynamic probe

References

- [1] Denton, J. D., and Johnson, C. G., 1976, "An Experimental Study of the Tip Leakage Flow Around Shrouded Turbine Blades," CEGB Research Report No. CEGB-R/M/N848.
- [2] Peters, P., Breisig, V., Giboni, A., Lerner, C., and Pfost, H., 2000, "The Influence of the Clearance of Shrouded Rotor Blades on the Development of the Flow Field and Losses in the Subsequent Stator," ASME Paper No. 2000-GT-478.
- [3] Hunter, S. D., and Manwaring, S. R., 2000, "Endwall Cavity Flow Effects on Gaspath Aerodynamics in an Axial Flow Turbine. 1. Experimental and Numerical Investigation," ASME Paper No. 2000-GT-651.
- [4] Wallis, A. M., Denton, J. D., and Demargne, A. A. J., 2001, "The Control of Shroud Leakage Flows to Reduce Aerodynamic Losses in a Low Aspect Ratio, Shrouded Axial Flow Turbine," *J. Turbomach.*, **23**, pp. 334–341.
- [5] Cao, C., Chew, J. W., Millington, P. R., and Hogg, S. I., 2003, "Interaction of Rim Seal and Annulus Flows in an Axial Flow Turbine," ASME Paper No. GT-2003-38368.
- [6] Anker, J. E., and Mayer, J. F., 2002, "Simulation of the Interaction of Labyrinth Seal Leakage Flow and Main Flow in an Axial Turbine," ASME Paper No. GT2002-30348.
- [7] Schlienger, J., Pfau, A., Kalfas, A. I., and Abhari, R. S., 2003, "Effects of Labyrinth Seal Variation on Multistage Axial Turbine Flow," ASME Paper No. GT2003-38128.
- [8] Pfau, A., Treiber, M., Sell, M., and Gyarmathy, G., 2001, "Flow Interaction From the Exit Cavity of an Axial Turbine Blade Row Labyrinth Seal," *J. Turbomach.*, **123**, pp. 342–352.
- [9] Pfau, A., Schlienger, J., Rusch, D., Kalfas, A. I., and Abhari, R. S., 2003, "Unsteady Flow Interactions Within the Inlet Cavity of a Turbine Rotor Tip Labyrinth Seal," ASME Paper No. GT2003-38128.
- [10] Sell, M., Schlienger, J., Pfau, A., Treiber, M., and Abhari, R. S., 2001, "The 2-Stage Axial Turbine Test Facility LISA," ASME Paper No. 2001-GT-492.
- [11] Treiber, M., Kupferschmid, P., and Gyarmathy, G., 1998, "Analysis of the Error Propagation Arising From Measurements With a Miniature Pneumatic 5-Hole Probe," *Proceedings of the 13th Symposium on Measuring Techniques in Cascades and Turbomachines*, Limerick, Ireland.
- [12] Pfau, A., Schlienger, J., Kalfas, A. I., and Abhari, R. S., 2003, "Unsteady, 3-Dimensional Flow Measurement Using a Miniature Virtual 4 Sensor Fast Response Aerodynamic Probe (FRAP)," ASME Paper No. GT2003-38128.
- [13] Dawes, W. N., 1998, "Blade Row Interference Effects in Axial Turbomachinery Stages: Simulation of Unsteady Blade Row Interaction With CFD: Background," VKI Lecture Series, February 9–12.
- [14] Gregory-Smith, D. G., Ingram, G., Jayaraman, P., Harvey, N. W., and Rose, M. G., 2001, "Non-Axisymmetric Turbine End Wall Profiling," *Proc. Inst. Mech. Eng., Part A*, **215**(A6), pp. 721–734.
- [15] Havakechian, S., and Greim, R., 1999, "Aerodynamic Design of 50 Per Cent Reaction Steam Turbines," *Development of Turbomachinery Design*, J. Denton, ed., IMechE, Professional Engineering Publishing, London.
- [16] Harvey, N. W., Brennan, G., Newman, D. A., and Rose, M. G., 2002, "Improving Turbine Efficiency Using Non-Axisymmetric End Walls: Validation in the Multi-Row Environment and With Low Aspect Ratio Blading," ASME Paper No. GT-2002-30337.